Analysis of thermal deformation behavior and workability of 37CrS4 special steel

Jingcheng Yang[1], Lizhong Wang[2]*, Mingzhe Xue[1]**

[1] *Clean Energy Automotive Engineering Center, School of Automotive Studies, Tongji University,*
4800 Cao'An Road, Shanghai 201804, P. R. China
[2] *State Key Laboratory of Mechanical Manufacturing System Engineering, School of Mechanical Engineering,*
Xi'an Jiaotong University, No. 28 Xianning West Road, Xi'an, Shaanxi 713599, P. R. China

Abstract

In order to optimize the thermal forging process of 37CrS4 special steel, single-pass thermal pressing tests are conducted, and a strain compensation Arrhenius constitutive equation is proposed based on the stress-strain curves of 37CrS4 at the temperature of 900–1100 °C and the strain rate of 0.1–10 s^{-1}. The stress values calculated from the equation are in good agreement with the counterparts in the thermal simulation compression test. The high correlation between the calculated and experimental data verifies the correctness of the strain compensation based on Arrhenius constitutive equation. According to the dynamic material model and instability criterion, the processing maps of 37CrS4 are established. It is concluded that 37CrS4 is more suitable for thermal working at a strain rate of 0.1–0.37 s^{-1} and temperature of 1000–1100 °C.

1. Introduction

37CrS4 is a kind of special steel imported from Germany, material No. 1.7038, which has high rupture strength and creep strength at high temperatures, good impact toughness at low temperatures, good hardenability, no overheating tendency, small quenching deformation, general plasticity at cold deformation and good machinability. Poor weldability, preheating before welding, and heat treatment after welding to eliminate stress, generally used after quenching and tempering, can also be used after medium and high-frequency surface quenching or quenching and low and medium temperature tempering [1, 2]. It is widely used for important structural parts under high load conditions, such as transmission parts of vehicles and engines, rotor, main shaft, transmission shaft under heavy load of the steam turbine generator, large section parts, forgings with higher strength and larger quenched and tempered section than 35CrMo steel, such as big gear for locomotive traction, transmission gear of supercharger, rack, rear axle, connecting rod

and spring clamp under great load. It can also be used for drill pipe joints and fishing tools in oil deep wells below 2000 m [3].

The constitutive model is often used to describe the physical properties of metal materials [4]. The commonly used constitutive models are Johnson-Cook (J-C) model, Zerilli-Armstrong (Z-A) model, and Arrhenius hyperbolic sine model. In the field of high-temperature plastic deformation of metal materials, Arrhenius constitutive model is known for its high prediction accuracy and is more suitable for high-temperature scenarios [5]. Yang et al. studied the hot deformation behavior of 9Cr3W3Co alloy steel. They calculated the thermal activation energy of 9Cr3W3Co alloy steel and obtained the constitutive equation of 9Cr3W3Co alloy steel [6]; Wang et al. studied the hot deformation behavior of 20Cr2Ni4A alloy steel and proposed the constitutive equation of strain compensation based on Arrhenius type equation and Zener-Hollomon parameter, which has high prediction accuracy [7]; Yang et al. studied the thermal deformation behavior of 25Cr2Ni4MoVA steel and

considered that there was a functional relationship between material constant and strain. The prediction accuracy of the constitutive model is improved by using the material constant expressed by the relation, including strain [8]. In previous work, we conducted a hot compression test on 20Cr steel, and obtained the constitutive equation of 20Cr through the linear fitting method, which provided theoretical support for the process selection of automobile gear [9].

However, the Arrhenius constitutive model does not consider the effect of strain on the accuracy of the constitutive equation. The peak stress is used to simply represent the high-temperature characteristics of metal materials at a certain temperature and strain rate. The actual error is large, which cannot meet the requirements of numerical simulation in the process of forging process development. In previous work, strain compensation was included in the Arrhenius constitutive equation and applied for the investigation of 3Cr-1Si-1Ni Ultra-High Strength Steel [10].

In view of the research on the high-temperature rheological properties of a material, the hot workability is discussed in an endless stream. Zhao et al. studied the hot deformation behavior of 1Cr12Ni2Mo2-WVNb martensitic stainless steel [11]. The processing maps of 1Cr12Ni2Mo2WVNb alloy steel under 0.3, 0.4, 0.5, and 0.6 strains were established, and the optimal hot working range of 1Cr12Ni2Mo2WVNb alloy steel was obtained. Ye et al. studied the hot deformation behavior of 25Cr2Ni4MoV alloy steel [12]. They superimposed the 2D processing map to draw the 3D processing map, classified the grain sizes of different processing areas, and discussed the hot working performance of 25Cr2Ni4MoV alloy steel. Li et al. discussed the hot deformation behavior of V-5Cr-5Ti alloy [13]. The flow stress curve with friction factor was corrected, and in-depth research on dynamic recrystallization and dynamic softening during hot deformation was conducted. Li et al. studied the hot deformation behavior of 9Ni590B alloy steel and found that the hot deformation microstructure was acicular martensite [14]. The correctness of the processing map was proved by analyzing the unsteady microstructure.

In summary, the research on high-temperature plastic properties of alloys has been studied in-depth in the flow stress model, hot workability, dynamic recrystallization, and so on. At present, precision plastic forming has become an important processing method for alloy products. Compared with traditional machining methods, precision plastic forming products do not damage metal flow lines, have high strength, and have less material waste [15, 16]. The cold plastic properties and fatigue properties of 37CrS4 at room temperature have been mainly reported in the existing literature. However, there are few reports on plastic deformation behavior and hot workability at high temperatures. As a kind of special steel with wide application

T a b l e 1. Contents of various chemical elements in 37CrS4 special steel (%, mass fraction)

C	Si	Mn	P	S	Cr
0.34–0.41	≤ 0.4	0.6–0.9	≤ 0.075	0.02–0.04	0.9–1.2

and excellent properties, the high-temperature plastic properties of 37CrS4 need to be studied and discussed urgently. In this paper, the hot deformation behavior of 37CrS4 is examined by a hot simulation compression test, and the hot workability of 37CrS4 is discussed. The results provide theoretical support for the finite element numerical simulation and process development of 37CrS4.

2. Materials and experimental process

The material used in the experiment was quenched and tempered 37CrS4 round bar, and the chemical composition of the material is shown in Table 1. The sample was turned into a cylinder with a size of $\varnothing\, 8 \times 12\,\text{mm}^2$, and the end face was polished to a roughness of Ra 1.6 by a grinder to prevent excessive test error caused by end face defects.

The experiment was carried out on a Gleeble-1500D thermal-mechanical simulator, and the heating rate of the test piece was $10\,°\text{C s}^{-1}$. After the sample was heated to $1200\,°\text{C}$, the heat preservation was carried out for 3 min to make the temperature distribution inside the sample uniform. The test temperature of the sample was reduced at $5\,°\text{C s}^{-1}$ to the thermal compression temperature, followed by a 30 s heat preservation. The thermal compression temperature was set at 900, 950, 1000, 1050, and $1100\,°\text{C}$, respectively, with a gap of $50\,°\text{C}$. The strain rate was set at 0.1, 1, and $10\,\text{s}^{-1}$, respectively. After the end of the experiment, the thermal compression deformation structure was maintained by water quenching. The temperature variation of the whole process of the thermal simulation compression experiment is shown in Fig. 1.

The chilled samples were cut along the axial direction with a cutting machine and polished with a grinding machine and polishing machine. Finally, a saturated picric acid aqueous solution was used to corrode the ground surface. The microstructure of 37CrS4 was observed with a metallographic microscope Nikon MA100.

3. Results and analysis

The flow stress curves obtained from thermal compression experiments show that the stress values fluctuate with the strain, which is related to the inter-
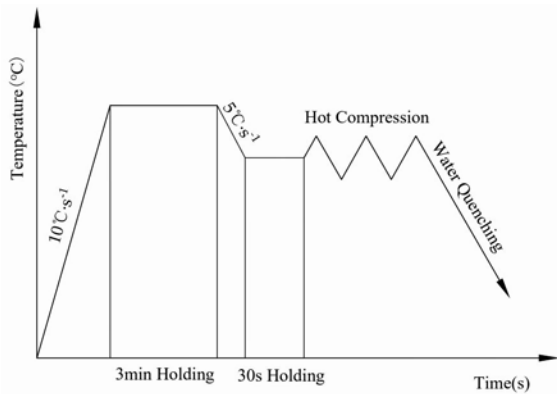
Fig. 1. Temperature curve of thermal compression experiment.

face friction. In order to correct the true stress-strain curve, the logarithm of stress is taken to correspond to the whole strain range. The slope between logarithmic stress and corresponding strain is calculated and averaged. Finally, according to the average slope, the stress of the upward warping section is corrected, and the accuracy is acceptable.

The true stress-strain curves of 37CrS4 at different temperatures and strain rates are shown in Fig. 2a, which shows a typical dynamic recrystallization phenomenon at the strain rate of $0.1\,s^{-1}$. When the strain is low, the growth rate of flow stress is very high due to work hardening and the softening effect caused by gradually enhanced dynamic recrystallization. The growth rate of flow stress slows down until the peak value of flow stress appears on the stress curve. After the effect of dynamic recrystallization reaches the peak stress, the flow stress of 37CrS4 special steel begins to decrease, which indicates the domination of dynamic recrystallization behavior. Afterward, the stress decreases to a constant value and remains basically stable. When the strain rate is $1\,s^{-1}$ (Fig. 2b), the higher the temperature, the more obvious the "single peak" effect of the stress curve of dynamic recrystallization, indicating a positive correlation between temperature and dynamic recrystallization. When the strain rate is $10\,s^{-1}$ (Fig. 2c), due to its high value, the accumulated dislocations in the metal have no time to annihilate, resulting in an increase in internal stress. There is no obvious "single peak effect" on the stress curve. The variation of peak stress with temperature is shown in
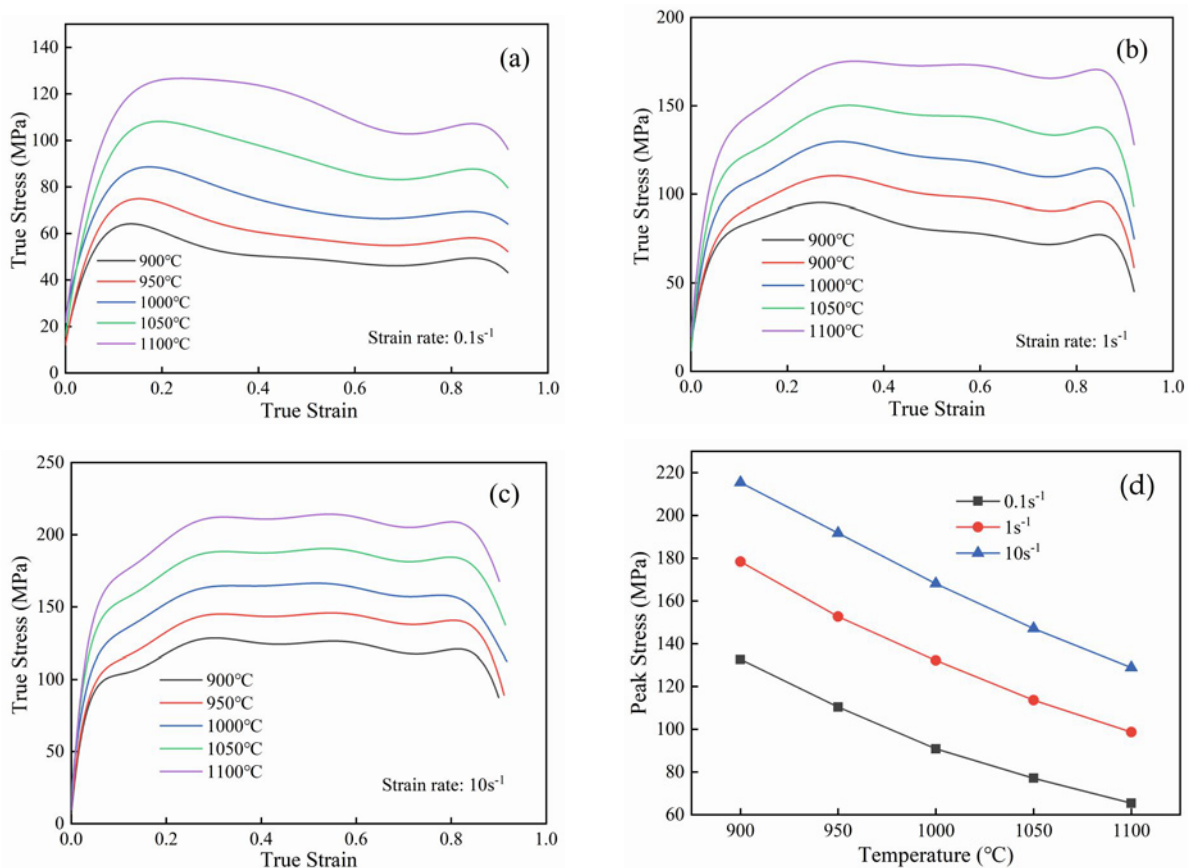

Fig. 2. Stress-strain curves of 37CrS4 special steel under different temperatures at strain rate of (a) $0.1\,s^{-1}$, (b) $1\,s^{-1}$, (c) $10\,s^{-1}$, and (d) variation of peak stress with temperature corresponding to different strain rates.
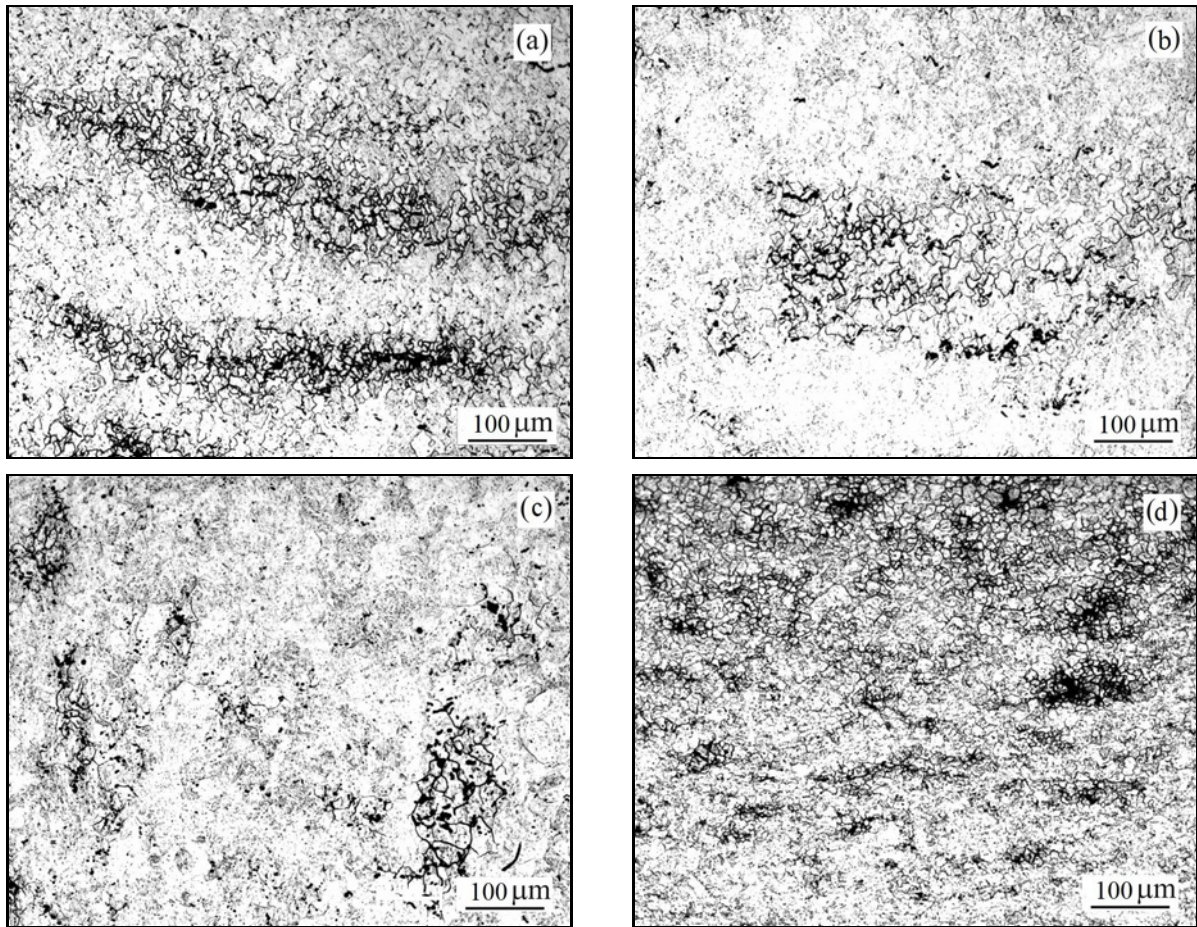
Fig. 3. The microstructures of the specimens at: (a) 900 °C, $\dot{\varepsilon} = 0.1\,\mathrm{s}^{-1}$, (b) 1000 °C, $\dot{\varepsilon} = 0.1\,\mathrm{s}^{-1}$, (c) 1100 °C, $\dot{\varepsilon} = 10\,\mathrm{s}^{-1}$, and (d) 1100 °C, $\dot{\varepsilon} = 0.1\,\mathrm{s}^{-1}$.

Fig. 2d. It can be observed that the temperature is negatively correlated with stress, and the strain rate is positively correlated with stress.

Figure 3 shows the microstructure of some 37CrS4 special steel specimens deformed at different temperatures and different strain rates. The true strain corresponding to all metallographic is 0.916. All specimens are etched with a saturated picric acid solution. It can be seen that the austenitic grain boundary corroded by saturated picric acid is clearly visible. The compression behavior causes the distortion of grain boundaries. In Figs. 3a–d, some smaller grains appear around the larger grains, which indicates the occurrence of dynamic recrystallization behavior during high-temperature plastic deformation of 37CrS4, and the incomplete dynamic recrystallization behavior. The dynamic recrystallization occurs at the inflection point of the stress curve, and the corresponding microstructure is that fine recrystallized grains begin to appear around the larger original grains. These grains have not grown up completely, which demonstrates the incompletion of the dynamic recrystallization process. In Figs. 3a–d, some black strip structures can also be found. Combined with the chemical com-

position of 37CrS4 special steel and the morphology of metallographic structure, these black strip structures are supposed to be sulfide.

4. Establishment and verification of constitutive equation

According to the previous research from Sellars and McTegart [17, 18], the Arrhenius flow stress constitutive equation, which can unambiguously and effectively reveal the thermal deformation phenomenon, is formulated and analyzed. The flow stress, temperature, and strain rate can be characterized by Eq. (1) in the form of activation energy Q and temperature T:

$$\dot{\varepsilon} = AF(\sigma)\exp\left(\frac{Q}{RT}\right), \qquad (1)$$

where Q is the activation energy of thermal deformation (kJ mol^{-1}), $F(\sigma)$ is the function of stress σ, R is the gas constant (8.314 J mol^{-1} K^{-1}), T is the temperature (K), A is material constant, and $\dot{\varepsilon}$ is strain rate (s^{-1}).
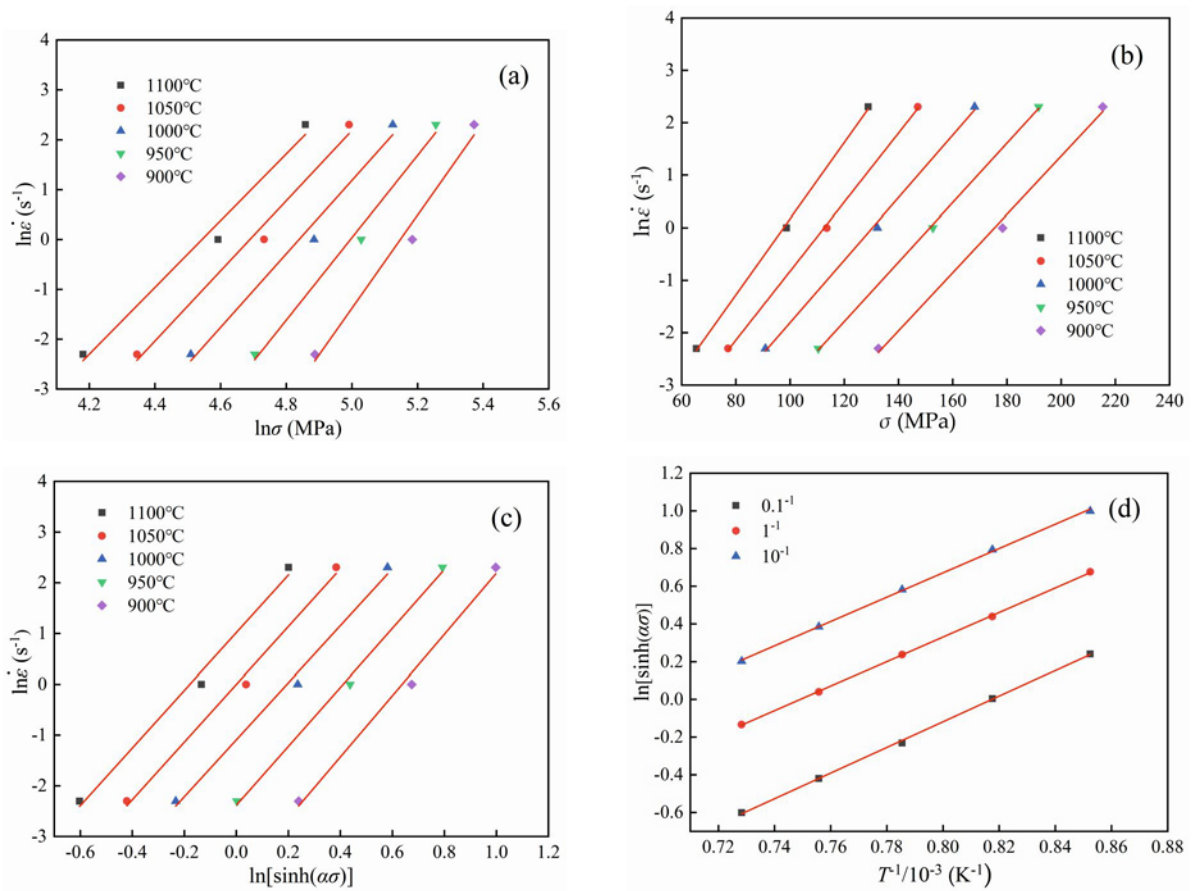
Fig. 4. The linear relationships of (a) $\ln\dot{\varepsilon} - \ln\sigma$, (b) $\ln\dot{\varepsilon} - \sigma$, (c) $\ln\dot{\varepsilon} - \ln[\sinh(\alpha\sigma)]$, and (d) $1000/T - \ln[\sinh(\alpha\sigma)]$.

$F(\sigma)$ is a function of stress σ, which is described as follows:

$$F(\sigma) = \sigma^{n_1} \qquad (\alpha\sigma < 0.8), \qquad (2)$$

$$F(\sigma) = \exp(\beta\sigma) \qquad (\alpha\sigma < 1.8), \qquad (3)$$

$$F(\sigma) = [\sinh(\alpha\sigma)]^n \qquad \text{(for all stress)}, \qquad (4)$$

where $\alpha = \beta/n_1$, σ is flow stress (MPa), β is material constant, and n, n_1 are strain hardening indexes.

According to the previous research from Zener and Hollomon [19, 20], when metal materials experience plastic deformation at high temperatures, the thermal activation process of thermal holds the strain rate, and the connection between strain rate and temperature can be characterized by Z parameter:

$$Z = \dot{\varepsilon}\exp\left(\frac{Q}{RT}\right) = A\left[\sinh(\alpha\sigma)\right]^n, \qquad (5)$$

where Z is temperature and strain rate modified co-efficient (Z parameter).

By substituting Eqs. (2), (3), and (4) into Eq. (1) and taking the natural logarithm of the left and right sides of three equations, the following Eqs. (6)–(8) are obtained:

$$\ln\dot{\varepsilon} = \ln A_1 + n_1\ln\sigma - \frac{Q}{RT}, \qquad (6)$$

$$\ln\dot{\varepsilon} = \ln A_2 + \beta\sigma - \frac{Q}{RT}, \qquad (7)$$

$$\ln\dot{\varepsilon} = \ln A + n\ln[\sinh(\alpha\sigma)] - \frac{Q}{RT}. \qquad (8)$$

$\ln\dot{\varepsilon} - \ln\sigma$ relationship curve and $\ln\dot{\varepsilon} - \sigma$ relationship curve are acquired by linear fitting means for Eqs. (6), (7), and (8), respectively, as shown in Figs. 4a,b. According to the average of the linear fitting slope of $\ln\dot{\varepsilon} - \ln\sigma$ relationship curve and $\ln\dot{\varepsilon} - \sigma$ relationship curve, $n_1 = 7.738766$, $\beta = 0.061972\,\text{MPa}^{-1}$, $\alpha = \beta/n_1 = 0.008007995073$ can be acquired.

The strain hardening coefficient $n = 5.76242$ can be solved from the relationship curve $\ln\dot{\varepsilon} - \ln[\sinh(\alpha\sigma)]$ in Fig. 4c. The computing method of activation energy is shown in Eq. (9):

$$Q = R\left|\frac{\partial\ln\dot{\varepsilon}}{\partial\ln[\sinh(\alpha\sigma)]}\right| \times \left|\frac{\partial\ln[\sinh(\alpha\sigma)]}{\partial(1000/T)}\right|. \qquad (9)$$

Substituting the average value of linear fitting slope acquired from Figs. 4c,d into Eq. (9), the activation energy Q of 37CrS4 can be computed to be
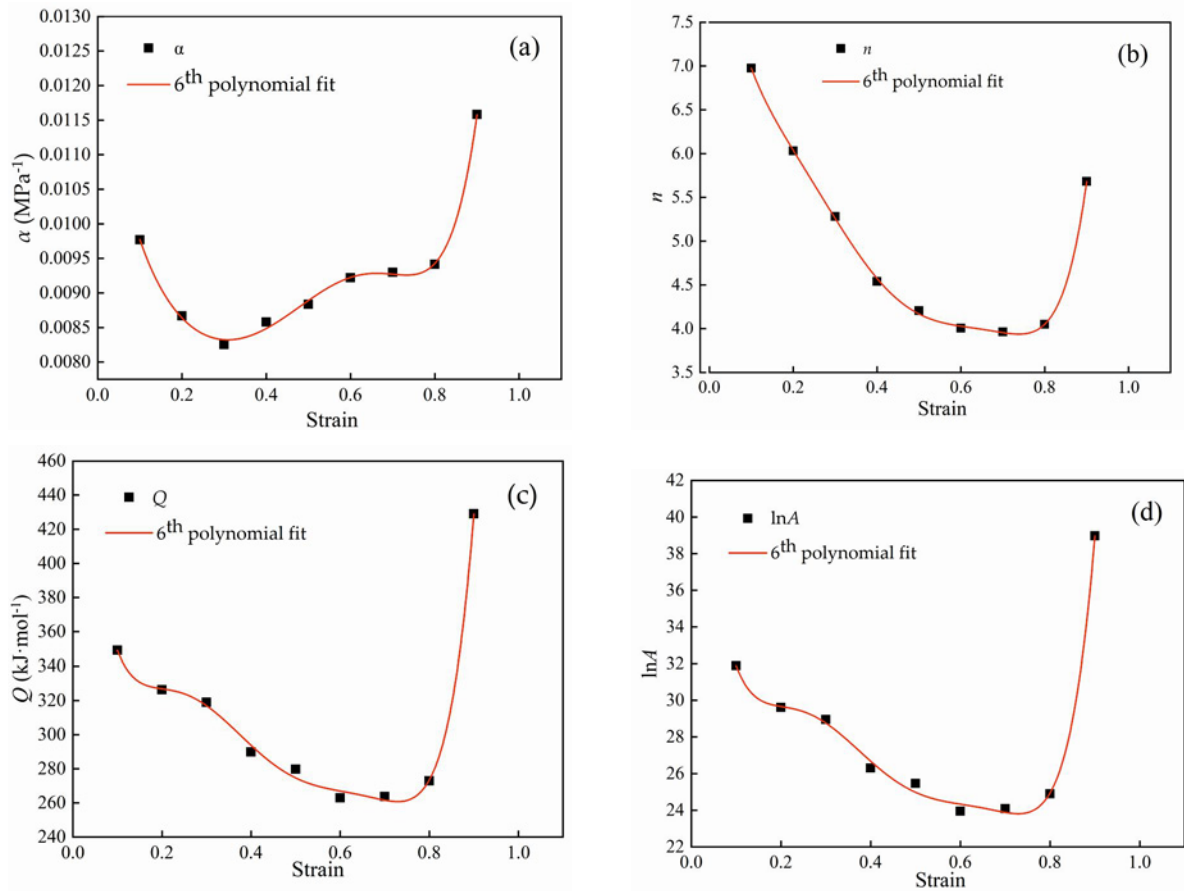
Fig. 5. Constitutive constants at various strains: (a) α, (b) n, (c) Q, and (d) ln$A$.

315.805 kJ mol^{-1}. Equation (7) can be acquired after Eq. (5) logarithm of treatment:

$$\ln \dot{\varepsilon} + \frac{Q}{RT} = \ln A + n \ln \left[\sinh \left(\alpha \sigma \right) \right]. \qquad (10)$$

Equation (10) reveals the linear connection of Fig. 4c, and the slope is $n = 5.76242$. The nodal increment of Eq. (10) is $\ln A - Q/RT$ while the average nodal increment can be obtained from Fig. 4c. Hence it can be calculated that $\ln A = 28.254481$, $A = 1.86537 \times 10^{12}$.

Based on the results obtained, the thermal deformation constitutive equation of 37CrS4 can be acquired by substituting various material constants into Eq. (8), which is shown in Eq. (11):

$$\dot{\varepsilon} = 1.86537 \times 10^{12} \left[\sinh \left(0.008\sigma \right) \right]^{5.76242} \cdot$$
$$\cdot \exp \left(-\frac{315805}{8.314T} \right). \qquad (11)$$

The traditional Arrhenius constitutive equation merely treats four material parameters as constants to describe the stress and strain at various temperatures

and strain rates. However, in fact, these four parameters are not constants and are variables accompanying strain changes [23, 24]. Therefore, it is necessary to import strain as an important parameter to modify Arrhenius constitutive equation.

According to the computing method of the traditional Arrhenius constitutive equation in the previous chapters, nine groups of strains are calculated in the range of strain $0.1 \sim 0.9$ with an interval of 0.1. The values of four material constants (α, n, Q, $\ln A$) under these nine groups of strains are calculated, and the polynomial fitting function relationship between strain ε and four material constants is established. The degree of polynomial plays a decisive role in the fitting accuracy. Literature [25] shows that the fitting of the sixth-degree polynomial can fully meet the accuracy requirements and is suitable for expressing the relationship between four material constants and strain.

For better verifying the precision of the constitutive equation, the stress values related to 1000 are used as the verification data set, and other data are used to structure the strain-compensated Arrhenius constitutive equation.

Figure 5 shows the functional relationship image of four material constants fitted by the sixth-degree

Table 2. Coefficients of polynomial fitting curves for material coefficients

	0	1	2	3	4	5	6
B	0.01	−0.04	0.20	−0.59	1.13	−1.18	0.49
C	9.33	−40.20	243.34	−920.97	1821.78	−1755.63	655.27
D	51.19	−389.85	2799.56	−9984.14	18303.24	−16654.07	5973.85
F	552.31	−4135.96	29992.35193	−107670.07	198180.85	−180839.24	65019.32

polynomial. It can be observed that the fitting accuracy of the sixth-degree polynomial is relatively high.

$$\sigma = \frac{1}{\alpha}\left\{\left(\frac{\dot{\varepsilon}\exp\left(\frac{Q}{RT}\right)}{A}\right)^{\frac{1}{n}} + \left[\left(\frac{\dot{\varepsilon}\exp\left(\frac{Q}{RT}\right)}{A}\right)^{\frac{2}{n}} + 1\right]\right\}$$

$$\alpha = B_0 + B_1\varepsilon + B_2\varepsilon^2 + B_3\varepsilon^3 + B_4\varepsilon^4 + B_5\varepsilon^5 + B_6\varepsilon^6$$
$$n = C_0 + C_1\varepsilon + C_2\varepsilon^2 + C_3\varepsilon^3 + C_4\varepsilon^4 + C_5\varepsilon^5 + C_6\varepsilon^6$$
$$\ln A = D_0 + D_1\varepsilon + D_2\varepsilon^2 + D_3\varepsilon^3 + D_4\varepsilon^4 + D_5\varepsilon^5 + D_6\varepsilon^6$$
$$\frac{Q}{1000} = F_0 + F_1\varepsilon + F_2\varepsilon^2 + F_3\varepsilon^3 + F_4\varepsilon^4 + F_5\varepsilon^5 + F_6\varepsilon^6.$$
(12)

The Arrhenius constitutive equation is sorted into the equation with Z parameter and the Z parameter is replaced by the product term containing Q in Eq. (5). Equation (12) embodies the strain compensation constitutive equation characterized by material constants (α, n, Q, $\ln A$), and also lists the fitting relations of four material constants. The coefficients of the sixth polynomial in Eq. (12) relative to the four material constants are presented in table form in Table 2.

To verify the prediction precision of strain compensation constitutive equation, the actual stress obtained from the thermal pressing experiment is compared with the flow stress computed by the strain compensation constitutive equation. Taking the stress value calculated by the model as the abscissa and the actual stress obtained by the thermal pressing test as the ordinate, the scatter diagram is drawn. The higher the prediction accuracy of the strain compensation transient equation is, the more scattering points of calculated stress and actual stress tend to be on the line of $y = x$. In this study, the prediction precision of the strain compensation constitutive equation is verified by testing the correlation between $y = x$ and stress scattering points.

Among them, the calculated values of rheological stresses for different strain are determined by various deformation conditions, calculated by Eq. (9).

Figure 6 represents the trend of the coordinate scatter of stress used $y = x$. It can be made out that the points are basically scattered around $y = x$. The correlation coefficient $R = 0.98563$. The mean relative error AARE (Average Absolute Relative Error) is
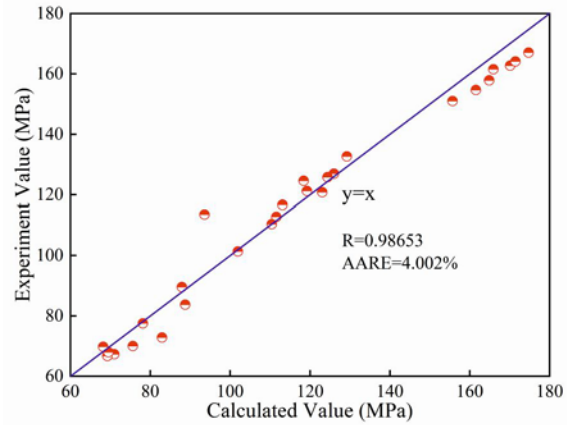

Fig. 6. Correlation between the experimental and predicted flow stresses.

4.002 %, which is less than 10 %, indicating that the error is small [27, 28]. The correlation coefficient and the mean relative error are calculated as shown in Eqs. (13) and (14):

$$R = \frac{\sum\limits_{i=1}^{N}\left(E_i - \bar{E}\right)\left(P_i - \bar{P}\right)}{\sqrt{\sum\limits_{i=1}^{N}\left(E_i - \bar{E}\right)^2}\sqrt{\sum\limits_{i=1}^{N}\left(P_i - \bar{P}\right)^2}} = 0.98563,$$
(13)

$$\text{AARE}\,(\%) = \frac{1}{N}\sum_{i=1}^{N}\left|\frac{E_i - P_i}{E_i}\right| \times 100\% = 4.002\%.$$
(14)

Evaluation indexes prove that the precision of the constructed 37CrS4 strain compensation instant on equation is high.

5. Processing maps

Processing maps are an efficient tool to characterize the thermal process performance of metal materials. The processing maps are composed of power dissipation maps and plastic instability maps. The contour line describes the power dissipation rate and divides the plastic instability region. The thermal process maps theory originates from the dynamic material model (DMM) proposed by Prasad et al. [16–19]. The
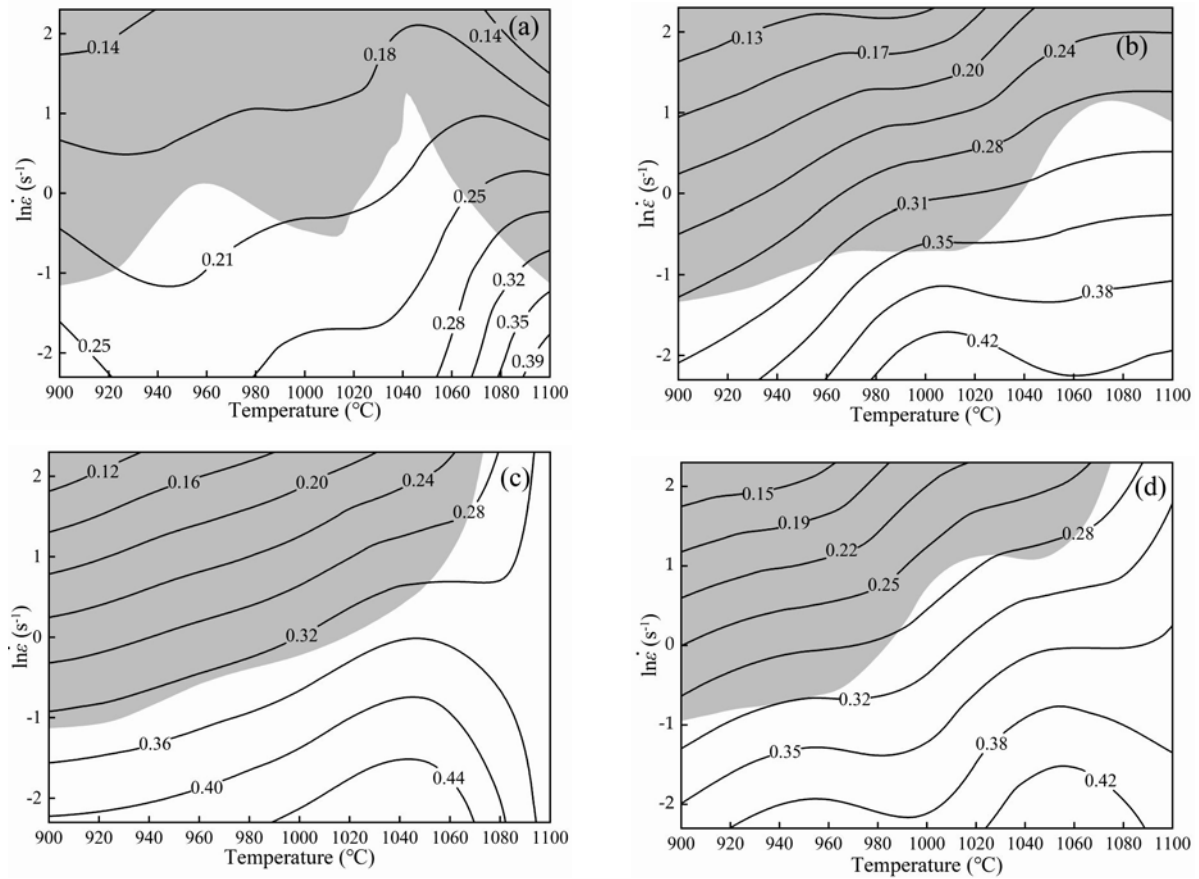
Fig. 7. Processing maps for the 37CrS4 special steel at strains of (a) 0.2, (b) 0.4, (c) 0.6, and (d) 0.8.

power dissipation maps describe the power dissipation under a certain strain. DMM theory reveals that the power absorbed by metal deformation is mainly composed of metal deformation and microstructure evolution. The power used by plastic deformation is denoted as G, and the power used by microstructure evolution is denoted as J. Connection between power absorbed by thermal deformation P and G, J, and the calculation relationship between the three indicators is shown in the Eq. (15):

$$P = \dot{\varepsilon}\sigma = G + J = \int_0^\varepsilon \sigma \mathrm{d}\dot{\varepsilon} + \int_0^\sigma \varepsilon \mathrm{d}\sigma. \quad (15)$$

Relationship between work hardening coefficient m and stress σ, strain rate is represented as follows [20–23]:

$$m = \frac{\partial(\ln \sigma)}{\partial(\ln \dot{\varepsilon})}. \quad (16)$$

Similarly, the relationship with the work hardening coefficient m and power dissipation rate η is shown in the Eq. (17) [24–26]:

$$\eta = \frac{J}{J_{\max}} = \frac{2m}{m+1}. \quad (17)$$

The thermal deformation of the alloy material not only includes recovery and recrystallization behavior, but also may exist plastic damage (such as adiabatic shear band, cracking, dendrite segregation, etc.). Hence, authors of [27–30] proposed the instability criteria, which supplemented the DMM theory:

$$\zeta(\dot{\varepsilon}) = \frac{\partial \ln\left(\dfrac{m}{m+1}\right)}{\partial \ln \dot{\varepsilon}} + m < 0. \quad (18)$$

The instability criterion assumes that $\zeta(\dot{\varepsilon}) < 0$, which means that this area is unstable. To improve the calculation accuracy of the work hardening coefficient m, the polynomial fitting method is used to obtain the work hardening coefficient m. In the thermal compression experiment of 37CrS4 special steel, each temperature corresponds to three different strain rates. According to the common sense of mathematics, the unique quadratic polynomial can be determined by the known coordinates of three points, and the correlation coefficient $R = 1$. Hence, for the calculation of the work hardening coefficient m, the quadratic polynomial fitting method has been able to meet the calculation accuracy requirements.

Figure 7 establishes the processing maps of 37CrS4 with strain rates of 0.1 to $10 \, \mathrm{s}^{-1}$ when the strain ε

is 0.2, 0.4, 0.6, and 0.8 in the temperature range of 900–1100 °C. The processing maps are obtained by composition of power dissipation map and instability criterion. The grey areas on the map are plastic deformation instability region. In Fig. 7a, when $\varepsilon = 0.2$, the maximum power dissipation rate is 0.39. The peak value appears at 1100 °C while the strain rate is 0.1 s^{-1}, which is located in the "irregular rectangular region" of 900–1100 °C and 0.37–10 s^{-1}. In Figure 7b, the peak area begins to expand and tends to spread to around 1000 °C, but it is still in the range of 1000–1100 °C with a strain rate of 0.1–0.22 s^{-1}, and the maximum power dissipation rate is 0.42. In Fig. 7c, the peak power dissipation rate reaches 0.44. The peak area is in the range of 1000–1070 °C with a strain rate of 0.1–0.25 s^{-1}. In Figure 7d, the maximum value of power dissipation rate is 0.42, and the peak area migrates to the high temperature area again, roughly in the temperature range of 1020–1090 °C, and the strain rate is 0.1–0.25 s^{-1}. When ε is 0.4, 0.6, and 0.8, corresponding to Figs. 7b–d, the unstable region is concentrated in the "irregular rectangular region" between 900 and 1000 °C, and the strain rate ranges from 0.37–10 s^{-1}. The unstable region (grey areas) decreases with the increase of strain when ε is 0.6 and 0.8, corresponding to Figs. 7c,d, the temperature is 1070–1100 °C, and the strain rate is 0.37–10 s^{-1}. For all four figures with a different strain, no instability region is observed when the strain rate is 0.1–0.37 s^{-1}. The greater the power dissipation rate is, the more power is used for microstructure evolution, the higher the possibility of recrystallization of the material, and the more suitable for thermoplastic processing. High temperature and low strain rate are considered to favor recrystallization.

6. Conclusions

In this work, thermal compression experiments of 37CrS4 special steel are conducted at the temperature of 900–1100 °C and the strain rate of 0.1–10 s^{-1}. "Single peak" effect observed on stress-strain curves indicates a positive correlation between temperature and dynamic recrystallization. The microstructure reveals that dynamic recrystallization does occur in 37CrS4 special steel, and the recrystallization is incomplete. A strain compensation Arrhenius constitutive equation is established, and the fitting of the sixth-degree polynomial with four material constants demonstrates high accuracy. Based on the power dissipation maps and the instability criterion, the processing maps of strain $\varepsilon = 0.2$, 0.4, 0.6, and 0.8 are structured. The instability region mainly distributes in the high strain rate range of 0.37–10 s^{-1}. The results show that the optimum technological parameters of 37CrS4 under the experimental conditions are:

strain rate 0.1–0.37 s^{-1}, temperature 1000–1100 °C.

References

[1] C. Kılıçaslan, U. İnce, Failure analysis of cold forged ^{37}Cr4 alloy M10x28 bolts, Eng. Fail. Anal. 70 (2016) 177–187. https://doi.org/10.1016/j.engfailanal.2016.08.006

[2] H. C. Ji, J. P. Liu, B. Y. Wang, X. F. Tang, J. G. Lin, Y. M. Huo, Microstructure evolution and constitutive equations for the high-temperature deformation of 5Cr21Mn9Ni4N heat-resistant steel, J. Alloys Compd. 693 (2017) 674–687. https://doi.org/10.1016/j.jallcom.2016.09.230

[3] K. H. Kloos, B. Fuchsbauer, J. Adelmann, Fatigue properties of specimens similar to components deep rolled under optimized conditions, Int. J. Fatigue 9 (1987) 35–42. https://doi.org/10.1016/0142-1123(87)90087-9

[4] X. Y. Fu, P. C. Bai, J. C. Yang, Hot deformation characteristics of 18Cr-5Ni-4Cu-N stainless steel using constitutive equation and processing map, Metals 10 (2020) 82. https://doi.org/10.3390/met10010082

[5] C. Renault, A. Y. Churyumov, A. V. Pozdniakov, T. A. Churyumova, Microstructure and hot deformation behavior of FeMnAlCMo steel, J. Mater. Res. Technol. 9 (2020) 4440–4449. https://doi.org/10.1016/j.jmrt.2020.02.069

[6] W. S. Yang, J. W. Wang, L. Jiang, T. J. Wang, Y. B Pei, Hot deformation behavior and processing maps of 9Cr3W3Co oxide dispersion-strengthened steel, High Temp. Mat. Process. 40 (2021) 23–31. https://doi.org/10.1515/htmp-2021-0010

[7] H. Wang, W. Wang, R. Zhai, R. Ma, J. Zhao, Z. Mu, Constitutive equations for describing the warm and hot deformation behavior of 20Cr2Ni4A alloy steel, Metals 10 (2020) 1169. https://doi.org/10.3390/met10091169

[8] J. Yang, Z. H. Su, F. L. Sui, Analysis on hot deformation and following cooling technology of 25Cr2Ni4MoVA steel, J. Iron Steel Res. Int. 28 (2021) 1305–1314. https://doi.10.1007/s42243-021-00580-8.

[9] J. C. Yang, P. T. Wang, L. Z. Wang, Z. J. Zhou, Study on warm precision forging method of integral combined gear, J. Xinjiang Univ. 37 (2020) 384–388. https://doi. 10.13568/j.cnki.651094.651316.2019.04.15.0002

[10] B. Lei, G. Chen, K. Liu, X. Wang, X. Jiang, J. Pan, Q. Shi, Constitutive analysis on high-temperature flow behavior of 3Cr-1Si-1Ni ultra-high strength steel for modeling of flow stress, Metals 9 (2019) 42. https://doi.org/10.3390/met9010042

[11] C. Zhao, J. Zhang, B. Yang, Y. F. Li, J. F. Huang, Y. Lian, Hot deformation characteristics and processing map of 1Cr12Ni2Mo2WVNb martensitic stainless steel, Steel Res. Int. 91 (2020) 2000020. https://doi.org/10.1002/srin.202000020

[12] L. Y. Ye, Y. W. Zhai, L. Y. Zhou, H. Z. Wang, P. Jiang, The hot deformation behavior and 3D processing maps of 25Cr2Ni4MoV steel for a super-large nuclear-power rotor, J. Manuf. Process 59 (2020) 535–544. https://doi.org/10.1016/j.jmapro.2020.09.062

[13] Y. M. Li, H. C. Ji, W. D Li, Y. G. Li, W. C. Pei, J. P. Liu, Hot deformation characteristics-constitutive equation and processing maps-of 21-4N heat-resistant steel, Materials 12 (2019) 89. https://doi.org/10.3390/ma12010089

[14] R. B. Li, Y. Q. Chen, C. X. Jiang, R. L. Zhang, Y. P. Feng, T. Huang, T. T. Chen, Hot deformation behavior and processing maps of a 9Ni590B steel, J. Mater. Eng. Perform. 29 (2020) 3858–3867. https://doi.org/10.1007/s11665-020-04907-6

[15] P. Zhang, C. Hu, Q. Zhu, C. G. Ding, H. Y. Qin, Hot compression deformation and constitutive modeling of GH4698 alloy, Mater. Design 65 (2015) 1153–1160. https://doi.org/10.1016/j.matdes.2014.08.045

[16] C. Zhang, L. W. Zhang, W. F. Shen, C. R. Liu, R. Q. Li, Study on constitutive modeling and processing maps for hot deformation of medium carbon Cr-Ni--Mo alloyed steel, Mater. Design 90 (2016) 804–814. https://doi.org/10.1016/j.matdes.2015.11.036

[17] S. H. Song, A comparison study of constitutive equation, neural networks, and support vector regression for modeling hot deformation of 316L stainless steel, Materials 13 (2020) 3766. https://doi.org/10.3390/ma13173766

[18] H. Wu, W. C. Xu, S. B. Wang, Z. Z. Yang, B. Guo, A cellular automaton coupled FEA model for hot deformation behavior of AZ61 magnesium alloys, J. Alloys Compd. 816 (2020) 152562. https://doi.org/10.1016/j.jallcom.2019.152562

[19] C. M. Sellars, W. J. McTegart, On the mechanism of hot deformation, Acta Metall. 14 (1966) 1136–1138. https://doi.org/10.1016/0001-6160(66)90207-0

[20] H. Shi, A. J. McLaren, C. M. Sellars, R. Shahani, R. Bolingbroke, Constitutive equations for high temperature flow stress of aluminium alloys, Met. Sci. J. 13 (1997) 210–216. https://doi.org/10.1179/mst.1997.13.3.210

[21] C. Zener, J. H. Hollomon, Effect of strain-rate upon the plastic flow of steel, J. Appl. Phys. 1 (1944) 22–27. https://doi.org/10.1063/1.1707363

[22] S. V. S. N. Murty, B. N. Rao, On the development of instability criteria during hot working with reference to IN 718, Mater. Sci. Eng. A 254 (1998) 76–82. https://doi.org/10.1016/S0921-5093(98)00764-3

[23] Z. B. Xiao, Q Wang, Y. Huang, J. Hu, M, Li, Hot deformation characteristics and processing parameter optimization of Al-6.32Zn-2.10Mg alloy using constitutive equation and processing map, Metals 11 (2021) 360. https://doi.org/10.3390/met11020360

[24] Y. J. Zhao, H. C. Ding, Y. F. Cao, P. L. Chen, Z. L. Hu, J. R. Zhang, L. X. Li, Hot processing map of an Al–4.30 Mg alloy under high one-pass deformation, Metals 11 (2021) 347. https://doi.org/10.3390/met11020347

[25] D. Pan, B. Liu, R. J. Xu, J. W. Qiu, C. X. Liu, Predicting workability of a low-cost powder metallurgical Ti-5Al-2Fe-3Mo alloy using constitutive modeling and processing map, Materials 14 (2021) 836. https://doi.org/10.3390/ma14040836

[26] C. J. Wang, L. Q. Zhang, S. Z. Wei, K. M. Pan, X. C. Wu, Q. K. Li, Preparation, microstructure, and constitutive equation of W-0.25 wt% Al_2O_3 alloy, Mater. Sci. Eng. A 744 (2019) 79–85. https://doi.org/10.1016/j.msea.2018.12.001

[27] M. Król, P. Snopiński, M. Pagáč, J. Hajnyš, J. Petrů, Hot deformation treatment of grain-modified Mg–Li alloy, Materials 13 (2020) 4557. https://doi.org/10.3390/ma13204557

[28] J. C. Yang, L. Z. Wang, Y. J. Zheng, Z. Z. Zhong, Strain modified constitutive equation and processing maps of high quality 20MnCr5(SH) gear steel, Crystals 11 (2021) 536. https://doi.org/10.3390/cryst11050536

[29] L. F. Cao, B. Liao, X. D. Wu, C. Y. Li, G. J. Huang, N. P. Cheng, Hot deformation behavior and microstructure characterization of an Al-Cu-Li-Mg-Ag alloy, Crystals 10 (2020) 416. https://doi.org/10.3390/cryst10050416

[30] M. Murugesan, M. Sajjad, D. W. Jung, Microstructure evaluation and constitutive modeling of AISI-1045 steel for flow stress prediction under hot working conditions, Symmetry 12 (2020) 782. https://doi.org/10.3390/sym12050782